processes

Article

A Modified Control Strategy for Three-Phase Four-Switch Active Power Filters Based on Fundamental Positive Sequence Extraction

Chun Xiao [1,2], Yulu Ren [1], Qiong Cao [1], Lei Wang [2,*] and Jingyu Yin [3]

[1] State Grid Shanxi Marketing Service Center, Taiyuan 030032, China; tyutxiaochun@163.com (C.X.); renyl_yx@126.com (Y.R.); caoqiong1122@sina.com (Q.C.)
[2] College of Electrical and Power Engineering, Taiyuan University of Technology, Taiyuan 030024, China
[3] Taiyuan Electric Power Supply Company of State Grid Shanxi Electric Power Company, Taiyuan 030001, China; cgy_sjf@126.com
* Correspondence: tywanglei1985@126.com

Abstract: Three-phase four-switch active power filters (APFs) have attracted attention due to their low amount of semiconductors and low cost. The traditional control strategy of three-phase four-switch APFs usually includes phase-locked loops (PLLs) and rotating coordinate transformation for harmonic detection, resulting in complicated calculations and increased computation. In this paper, a modified control strategy for three-phase four-switch APFs based on fundamental positive sequence extraction is proposed, eliminating PLLs and rotating coordinate transformation with trigonometric calculations. Harmonic extraction is based on the fundamental positive sequence extraction method, while non-locked phase loop coordinate transformation is proposed to eliminate trigonometric calculations. Quasi-PR control is adopted for current tracking, and DC voltage control is designed to suppress voltage imbalance between the two split capacitors on the DC side. The space vector pulse width modulation (SVPWM) method is modified for a reduced-switch APF topology. The proposed control strategy guarantees excellent harmonic compensation: harmonic currents are significantly suppressed when the APFs are working, the THD of the source current decreases to 3.86%, the bus voltage fluctuation on the DC side is small, the voltage remains stable, and the computational complexity is reduced. Finally, a simulation and an experimental hardware platform are established to validate the feasibility and performance of the proposed control strategy. The experimental results show that it has good performance in suppressing harmonics and improving power quality.

Keywords: three-phase four-switch APF; phase-locked loop; fundamental positive sequence extraction

check for updates

Citation: Xiao, C.; Ren, Y.; Cao, Q.; Wang, L.; Yin, J. A Modified Control Strategy for Three-Phase Four-Switch Active Power Filters Based on Fundamental Positive Sequence Extraction. *Processes* **2024**, *12*, 2586. https://doi.org/10.3390/pr12112586

Academic Editor: Wen-Jer Chang

Received: 29 September 2024
Revised: 7 November 2024
Accepted: 11 November 2024
Published: 18 November 2024

1. Introduction

Recently, smart grids and new energy generation technologies have developed rapidly, with new load types such as electric vehicles, virtual power plants, distributed energy storage, and so on being widely used. This is convenient for daily life, but also leads to effects such as transient high-voltage flickers and high-frequency noise during equipment startup [1,2], damaging the electronic components. Harmonics are also generated by the nonlinear aspects of loads, resulting in power quality degradation and increased grid losses [3,4]. Therefore, harmonic elimination in power systems has gradually received widespread attention [5]. Ref. [6] proposed a generalized instantaneous reactive power theory for reactive and harmonic current compensation, based on which an immediate reactive power compensator was proposed that is able to eliminate the harmonic currents caused by the instantaneous imaginary power [7]. APFs have become an important means of improving grids' power quality due to their excellent immediate compensation performance and rapid dynamic response, as well as their ability to effectively suppress noise and interference [8,9].

APFs are an effective approach to achieve harmonic suppression and dynamic reactive power compensation. As such, they have been widely researched and applied due to their outstanding advantages [10,11]. Ref. [12] proposed an EMTP-based active filter model to analyze the performance of active filters. In reality, APF performance is dependent on the control strategies adopted, which include P-Q theory, repetitive control, neural network control, and model predictive control, among others.

Refs. [13,14] presented a P-Q suppression harmonic control method based on instantaneous reactive power theory (IRPT). This method extracts harmonic components from load currents, an important step to improve APF performance. Ref. [15] presented the application of a generalized robust logarithmic family (GRLF) framework-derived least absolute difference (LAD) algorithm implemented in active power filters (APFs) for PQ enhancement, successfully eliminating lower- and higher-order errors from harmonically rich nonlinear load currents, resulting in accurate fundamental component extraction. Ref. [16] proposed a direct-current control strategy based on the synchronous rotating coordinate system, which achieves static-free tracking control of the grid current through a PI controller. Refs. [17,18] proposed an adaptive quantum calculus-based least mean fourth (q-LMF) control for shunt APFs, which maintains the source current's unity power factor while turning the former sinusoidal. Ref. [19] proposed a new version of the integral power theory in the $\alpha-\beta$ reference frame, combining the advantages of well-known instantaneous and integral power theories, as well as a shunt active-filtering strategy based on them. Ref. [20] presented finite-control set–model-predictive control (FCS-MPC) for hybrid APFs, improving their dynamic performance. Ref. [21] proposed an effective model-predictive control (MPC) method for SAPFs, avoiding the weighting factor and additional constraints of DC capacitor voltages in the cost function. In another study, neural network algorithms were employed in APFs to improve system performance [22]. In [23], particle swarm optimization (PSO) was proposed to improve the PI controller and enhance the dynamic response. Ref. [24] proposed a genetic algorithm (GA)-optimized fractional order proportional resonant controller (FOPRC) for SAPF current control. Ref. [25] presented a fuzzy logic controller for APFs with robust control capabilities. Meanwhile, Ref. [26] developed a Kalman filter-based super-twisting sliding mode control (SMC) for APFs. Ref. [27] proposed a global fast super-twisting terminal sliding-mode controller (GFSTTSMC) based on an adaptive recurrent Chebyshev fuzzy neural network for APFs. Finally, Ref. [28] proposed a direct power method based on modified interconnection and damping assignment passivity-based control (IDA-PBC).

Most APFs use six-switch or four-bridge arm eight-switch topologies [29]. They are complicated in terms of their control, large size, and high cost, and unfavorable for daily life applications. In recent years, the four-switch topology of three-phase converters, which has four power semiconductors instead of six switches, has attracted attention due to its advantageous simple structure and low, economical cost [30,31]. Ref. [32] proposed a novel two-leg VSI topology for a three-phase APF to reduce the cost and size. Ref. [33] presented a three-phase four-switch APF with a synchronous reference frame control strategy. The methods employed in four-switch APF systems are commonly based on P-Q theory. PLLs are included, and the a–b–c frame is transformed into a d–q–o frame through Park transformations, increasing computational demands. Ref. [34] presented a novel control method to improve APF performance with a PI plus vector PI controller; however, unbalanced capacitor voltages were not considered, and a Park transformation based on trigonometric computation was included, requiring long execution times. Ref. [35] removed two current sensors in APFs but still required a PLL for the voltage phase and employed traditional hysteresis control.

Besides common control methods, some novel control strategies have been developed to improve three-phase reduced-switch APFs' performance. Ref. [36] presented finite-control set model-predictive current control (FCS-MPCC) for four-switch APFs, adopting a prediction algorithm instead of the traditional control technique. Meanwhile, Ref. [37] proposed a one-cycle control method for reduced-switch APFs, removing the reference current generation. This control method is quite simple compared to most strategies, but its performance worsens when grid voltages deteriorate. In the literature [38,39], double-band hysteresis and three-level hysteresis control methods are proposed for four-switch APFs, as well as a modified modulation technique based on output signal identification [40]. However, these novel control strategies are complicated to implement and increase computation.

Among them, MPCC establishes a predictive model and employs an adaptive notch filter (ANF) to obtain the control references, avoiding the PLL. However, it requires a predictive model to calculate future states and evaluate all possible switching states to select the optimal solution, which increases its computational complexity. The OCC method can be implemented without a PLL, but its performance is significantly affected by grid voltage fluctuations. The HCC method removes the PLL by regulating the compensation current in the a–b–c coordinate frame, but introduces additional control logic and parameter adjustments, increasing system complexity. Additionally, its performance is largely dependent on settings such as the hysteresis width and high and low thresholds, meaning that small changes in these parameters may affect the stability of the system.

This paper proposes a modified control strategy for three-phase four-switch APFs based on fundamental positive sequence extraction, which removes the PLL and Park transformation. The harmonic extraction is designed based on the fundamental positive sequence extraction method, while the non-locked phase loop coordinate transformation method is proposed to eliminate trigonometric calculations. The mode of quasi-PR control is adopted for current tracking, and the SVPWM is developed for a reduced-switch APF topology. This control strategy has good harmonic suppression performance, validated, alongside its feasibility, through simulations and experiments on an experimental hardware platform.

2. Topology of Three-Phase Four-Switch APFs

Figure 1 shows the topology of three-phase four-switch shunt APFs. v_{sa}, v_{sb}, and v_{sc} represent the three-phase voltage; i_{sa}, i_{sb}, and i_{sc} are the three-phase current; i_{la}, i_{lb}, and i_{lc} are the three-phase load current; i_a, i_b, and i_c are the current of three-phase four-switch APFs; L is the inductor; U_{dc} is the bus voltage; meanwhile, u_{c1} and u_{c2} are the capacitor voltage. The two-phase bridge arms are composed of the power device's IGBT. Finally, S_1, S_2, S_3, and S_4 represent the switches.

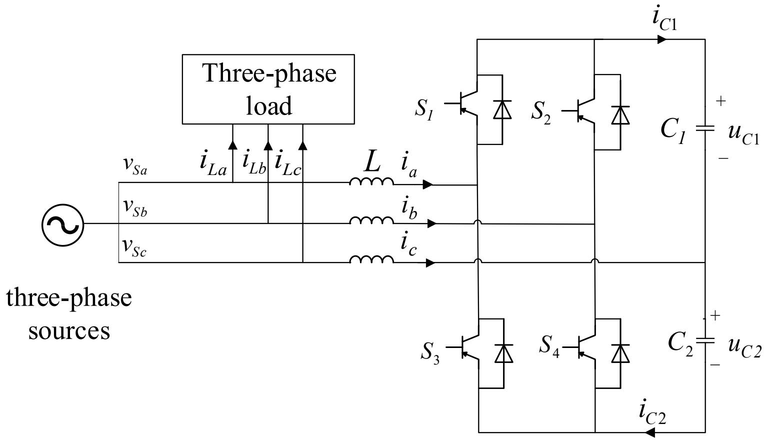

Figure 1. Topology of a three-phase four-switch APF.

3. Control Strategy for Three-Phase Four-Switch APFs

3.1. Fundamental Positive Sequence Extraction Method

The dq0 rotating coordinate detection method can effectively detect voltage harmonics, fluctuations, and distortion in the power grid, among others. However, this method involves a large number of trigonometric function transformations, making it prone to errors and a slow system response. In this paper, a control strategy for a stationary coordinate system is proposed to avoid complex coordinate transformations and remove the PLL to extract the grid voltage phase.

The commonly used method for fundamental positive sequence extraction is the synchronous reference frame (SRF). First, the three-phase load current is transformed from the a–b–c coordinate frame to the d–q coordinate frame by a Park transformation. In the d–q coordinate system, the fundamental positive sequence component of the current is transformed into a direct current, which can be extracted by filtering with a first-order low-pass filter (LPF). The transfer function of the first-order LPF is as follows:

$$H_{dq}(s) = \frac{\omega_c}{s + \omega_c} \tag{1}$$

where ω_c is the cutting frequency in the LPF. Although the SRF method achieves good extraction results, its calculations are relatively complex and require the participation of a PLL. In contrast, converting the LPF from the rotating d–q coordinate frame to the stationary a–b–c coordinate frame, which corresponds to the stationary reference frame (StatRF) control method, is simpler and easier to implement, making it more suitable for three-phase four-switch APFs.

Figure 2 shows a fundamental positive sequence extraction scheme, wherein the three-phase current is converted from the a–b–c coordinate frame to the d–q coordinate frame. The active and reactive components of the three-phase current can be given, obtaining the fundamental components through the LPF. Finally, the fundamental components under the a–b–c coordinate frame are obtained via inverse coordinate transformation.

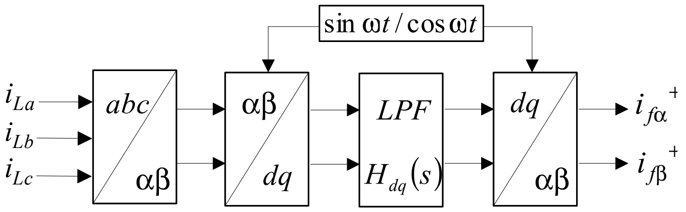

Figure 2. Schematic diagram of fundamental positive sequence extraction.

The equation from the a–b–c coordinate system to the α–β coordinate system is the following:

$$C_{32} = \frac{2}{3}\begin{bmatrix} 1 & -\frac{1}{2} & -\frac{1}{2} \\ 0 & \frac{\sqrt{3}}{2} & -\frac{\sqrt{3}}{2} \end{bmatrix} \tag{2}$$

Then, the following is true:

$$\begin{bmatrix} i_\alpha \\ i_\beta \end{bmatrix} = \frac{2}{3}\begin{bmatrix} 1 & -\frac{1}{2} & -\frac{1}{2} \\ 0 & \frac{\sqrt{3}}{2} & -\frac{\sqrt{3}}{2} \end{bmatrix} \begin{bmatrix} i_a \\ i_b \\ i_c \end{bmatrix} \tag{3}$$

The transformation from the α–β coordinate frame to the d–q coordinate frame is the following:

$$\begin{bmatrix} i_d \\ i_q \end{bmatrix} = \begin{bmatrix} \cos\theta & \sin\theta \\ -\sin\theta & \cos\theta \end{bmatrix} \begin{bmatrix} i_\alpha \\ i_\beta \end{bmatrix} \tag{4}$$

The LPF is converted from the d–q frame to the α–β frame, represented by the following equation:

$$H_{\alpha\beta}(s) = \frac{1}{2}\begin{bmatrix} \begin{pmatrix} H_{dq}(s + j\omega_o) \\ +H_{dq}(s - j\omega_o) \end{pmatrix} & \begin{pmatrix} jH_{dq}(s + j\omega_o) \\ -jH_{dq}(s - j\omega_o) \end{pmatrix} \\ \begin{pmatrix} -jH_{dq}(s + j\omega_o) \\ +jH_{dq}(s - j\omega_o) \end{pmatrix} & \begin{pmatrix} H_{dq}(s + j\omega_o) \\ +H_{dq}(s - j\omega_o) \end{pmatrix} \end{bmatrix} \tag{5}$$

Substituting (1) into (5), $H_{\alpha\beta}$(s) is derived as follows:

$$H_{\alpha\beta}(s) = \begin{bmatrix} \frac{\omega_c s + {\omega_c}^2}{(s+\omega_c)^2 + {\omega_0}^2} & \frac{\omega_c \omega_0}{(s+\omega_c)^2 + {\omega_0}^2} \\ \frac{-\omega_c \omega_0}{(s+\omega_c)^2 + {\omega_0}^2} & \frac{\omega_c s + {\omega_c}^2}{(s+\omega_c)^2 + {\omega_0}^2} \end{bmatrix} \quad (6)$$

Then, the transfer function of the LPF in the α–β frame is given by the following:

$$\begin{bmatrix} {i_{\alpha f}}^{+} \\ {i_{\beta f}}^{+} \end{bmatrix} = \begin{bmatrix} 0 & 1 \\ \frac{\sqrt{3}}{2} & -\frac{1}{2} \end{bmatrix} H_{\alpha\beta}(s) = \begin{bmatrix} \frac{-\omega_c \omega_0}{(s+\omega_c)^2 + {\omega_0}^2} & \frac{\omega_c s + {\omega_c}^2}{(s+\omega_c)^2 + {\omega_0}^2} \\ \frac{\frac{1}{2}\left(\omega_c \omega_0 + \sqrt{3}{\omega_c}^2 + \sqrt{3}\omega_c s\right)}{(s+\omega_c)^2 + {\omega_0}^2} & \frac{\frac{1}{2}\left(\omega_c \omega_0 - {\omega_c}^2 - \omega_c s\right)}{(s+\omega_c)^2 + {\omega_0}^2} \end{bmatrix} \quad (7)$$

The distortion current is calculated using Equation (7) to obtain the fundamental positive sequence current, that is, ${i_{\alpha f}}^{+}$, ${i_{\beta f}}^{+}$.

3.2. Coordinate Transformation Method Without PLLs

Conventional rotary coordinate transformation requires phase-locked loops to obtain the voltage's angular frequency information, and the error in the initial phase angle of the voltage leads to inaccurate detection signals. In this paper, the d–q components are obtained by directly calculating the rotational quantities, $\sin(\omega t + \phi)$ and $\cos(\omega t + \phi)$ of the transformation equation from the α–β frame to the d–q frame, ensuring that the elements in the following equation can accurately reflect the voltage phase:

$$\begin{bmatrix} u_\alpha \\ u_\beta \end{bmatrix} = C_{32} \begin{bmatrix} u_a \\ u_b \\ u_c \end{bmatrix} = \sqrt{\frac{2}{3}} \begin{bmatrix} 1 & -\frac{1}{2} & -\frac{1}{2} \\ 0 & \frac{\sqrt{3}}{2} & -\frac{\sqrt{3}}{2} \end{bmatrix} \begin{bmatrix} u_a \\ u_b \\ u_c \end{bmatrix} \quad (8)$$

The three-phase voltage is represented as follows:

$$\begin{cases} u_a = \sqrt{2}U \sin\theta \\ u_b = \sqrt{2}U \sin\left(\theta - \frac{2}{3}\pi\right) \\ u_c = \sqrt{2}U \sin\left(\theta + \frac{2}{3}\pi\right) \end{cases} \quad (9)$$

where U is the rms value of the grid voltage, determined as

$$\begin{bmatrix} u_\alpha \\ u_\beta \end{bmatrix} = C_{32} \begin{bmatrix} u_a \\ u_b \\ u_c \end{bmatrix} = \begin{bmatrix} \sqrt{3}U \sin\theta \\ \sqrt{3}U \cos\theta \end{bmatrix} \quad (10)$$

with

$${u_\alpha}^2 + {u_\beta}^2 = 3U^2 \quad (11)$$

$$U = \sqrt{\frac{{u_\alpha}^2 + {u_\beta}^2}{3}} \quad (12)$$

Substituting the above into Equation (10) yields the following:

$$\begin{cases} \sin\theta = \frac{u_\alpha}{\sqrt{3}U} = \frac{u_\alpha}{\sqrt{{u_\alpha}^2 + {u_\beta}^2}} \\ \cos\theta = \frac{u_\beta}{\sqrt{3}U} = \frac{u_\beta}{\sqrt{{u_\alpha}^2 + {u_\beta}^2}} \end{cases} \quad (13)$$

Then, the active and reactive voltage components in the d–q coordinate axis are determined as follows:

$$\begin{bmatrix} u_d \\ u_q \end{bmatrix} = \begin{bmatrix} \cos\theta & \sin\theta \\ -\sin\theta & \cos\theta \end{bmatrix} \begin{bmatrix} u_\alpha \\ u_\beta \end{bmatrix} = \begin{bmatrix} \frac{2u_\alpha u_\beta}{{u_\alpha}^2+{u_\beta}^2} \\ \frac{{u_\beta}^2-{u_\alpha}^2}{{u_\alpha}^2+{u_\beta}^2} \end{bmatrix} \tag{14}$$

Therefore, the PLL can be removed to avoid phase angle error, achieving the coordinate's transformation without PLL.

3.3. Quasi-PR Control Strategy

The PI regulator is generally able to accurately track the reactive current because the fundamental component is converted into a DC component in the d–q synchronous rotating coordinate system. PI control always achieves a steady-state error of zero but has poor performance in AC control systems, failing to deliver the expected results.

In our methodology, a PR controller is employed, and resonant controllers are designed according to each harmonic frequency. It has high gain at the designed frequency and can regulate the grid-side current as a standard sinusoidal waveform.

The approximation PR controller transfer function is as follows:

$$G_{PR}(s) = \frac{1}{2}[G_{PI}(s + j\omega_0) + G_{PI}(s - j\omega_0)] = K_p + \frac{K_i s}{s^2 + \omega^2{}_0} \tag{15}$$

where K_p and K_r are the proportional and resonant gain coefficients, respectively, and ω_0 is the resonant frequency. Undoubtedly, the resonant element is the core of the PR controller, which has near-infinite gain at ω_0 and low gain at other frequencies, effectively eliminating interfering signals. Figure 3 shows the Bode plot of the PR controller.

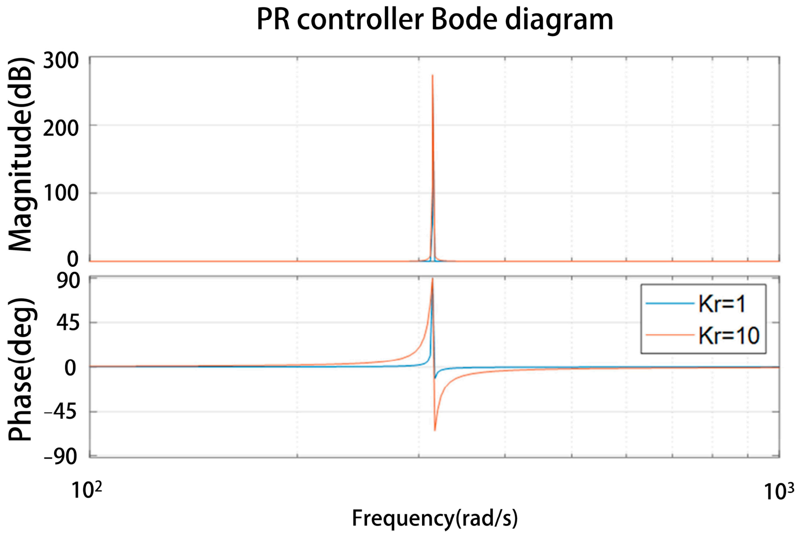

Figure 3. Bode plot of the PR control.

The ideal PR controller is fully capable of tracking AC quantities corresponding to the frequency. However, the frequency bandwidth near the resonance frequency is too narrow, and the gain at ω_0 is too high, making the system not stable enough. The PR controller would not be able to work accurately at the frequency in question with slight shifts in the AC signal. Although the bandwidth could be increased via adjustments, this would significantly increase the gain and phase changes, causing system instability. To improve the ability of the PR controller, the improved transfer function is as follows:

$$G_{PR}(s) = K_p + \frac{2K_r\omega_c s}{s^2 + 2\omega_c s + \omega^2{}_0} \tag{16}$$

where ω_c is the cut-off frequency. Meanwhile, the gain function of the quasi-PR controller is as follows:

$$|G_{PR}(s)|_{s=j\omega_0} = K_p + K_r \tag{17}$$

According to the above, when the input signal frequency is ω_0, the gain is $K_p + K_r$. Figure 4 shows the plot of the quasi-PR controller.

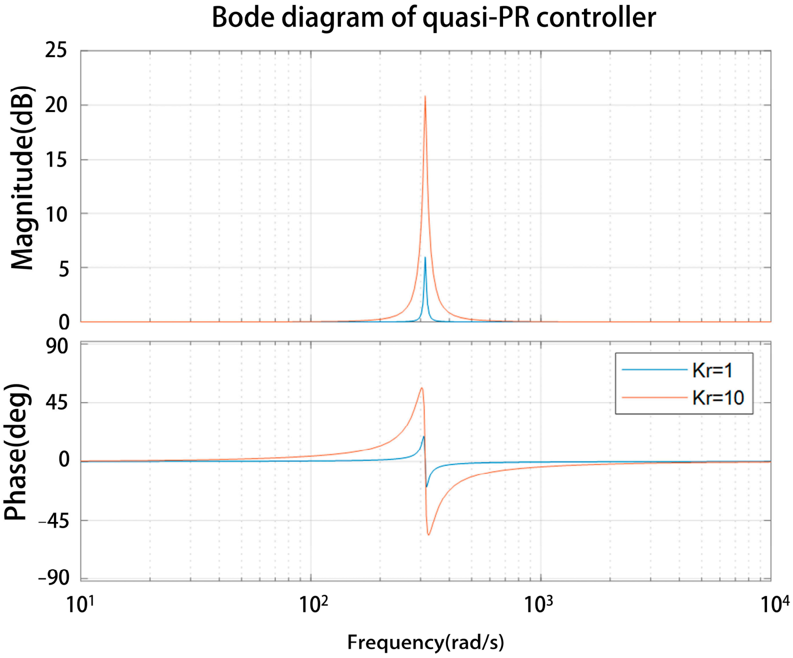

Figure 4. Bode plot of the quasi-PR controller.

Separate comparisons were carried out with different K_p, K_r, and ω_c to analyze the effect of diverse parameters on the controller, as shown in Figure 5.

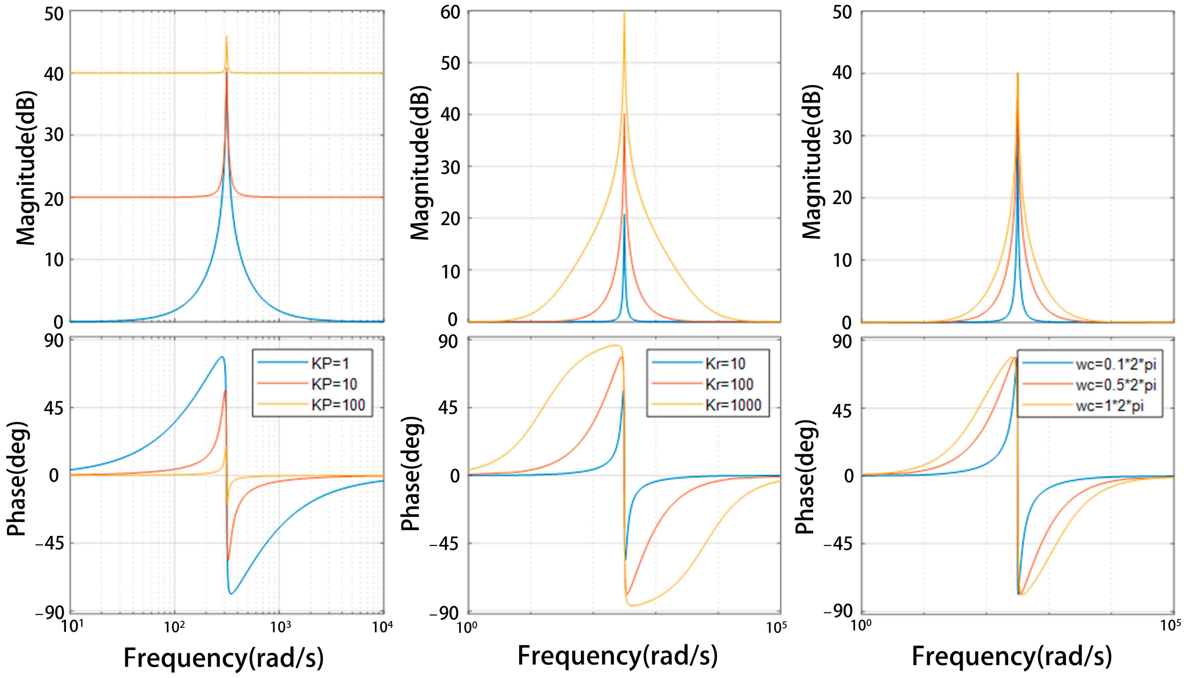

Figure 5. PR control comparisons with different parameters.

K_p increases alongside the overall gain and can regulate the system dynamics. According to the transfer function, the PR controller's gain at ω_0 is no longer infinite but rather $20\log(K_p + K_r)$. When K_p and ω_c are the same, the controller's gain increases alongside K_r and the bandwidth near the resonant frequency. Therefore, K_r is adjusted to allow the quasi-PR controller to have sufficiently large gain to achieve a steady error of zero.

When K_p and K_r are the same, ω_c increases to improve the bandwidth and the response speed. However, this may introduce high-frequency noise. There is a frequency fluctuation of ±0.5 Hz in the power grid, and the corresponding cut-off frequency is ω_{cmax} = 3.14 rad/s. The value of ω_c is generally set to 0.628 rad/s.

3.4. DC Voltage Control Strategy

We studied the stabilization of the DC bus voltage's impact on APF compensation performance. The DC voltage should be regulated and controlled to guarantee APF operation, according to the principle shown in Figure 6.

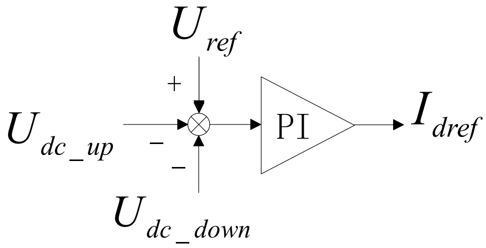

Figure 6. Schematic diagram of DC bus voltage control.

The error between the reference value and the measure of the DC voltage is fed into the PI controller. The component I_{dref}, the PI controller output, is added to the active component, obtaining the compensation current to keep the DC voltage stable.

DC midpoint voltage deviations affect the voltage balance of the APF capacitor, worsening the harmonic compensation performance and threatening normal APF operation. To avoid this problem, DC midpoint voltage deviations should be suppressed effectively.

The relationship between the DC current and the midpoint voltage is the following:

$$\begin{cases} i_{C1} = C1\frac{d(U_{C1}-U_n)}{dt} \\ i_{C2} = C2\frac{d(U_n-U_{C2})}{dt} \end{cases} \tag{18}$$

where the current on the DC side is i_{C1} and i_{C2}, and the midpoint voltage is U_n.

Then, if $C_1 = C_2 = C$, we obtain the following:

$$\frac{dU_n}{dt} = -\frac{i_{C1} - i_{C2}}{2C} \tag{19}$$

The equation, derived by Laplace transformation, is the following:

$$\begin{cases} U_n = \frac{i_{C1}-i_{C2}}{2sC} \\ G_c(s) = \frac{1}{2sC} \end{cases} \tag{20}$$

To achieve satisfactory anti-interference capabilities, PI control is employed, and the compensation method is shown in Figure 7.

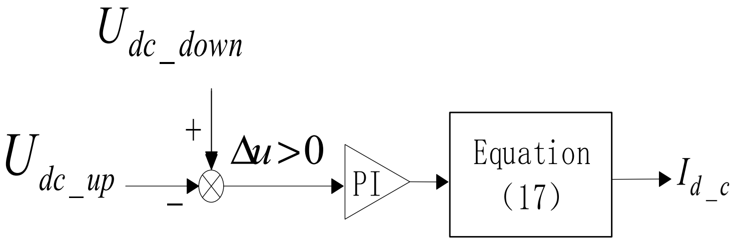

Figure 7. Schematic diagram of midpoint voltage control.

The overall control scheme is shown in Figure 8.

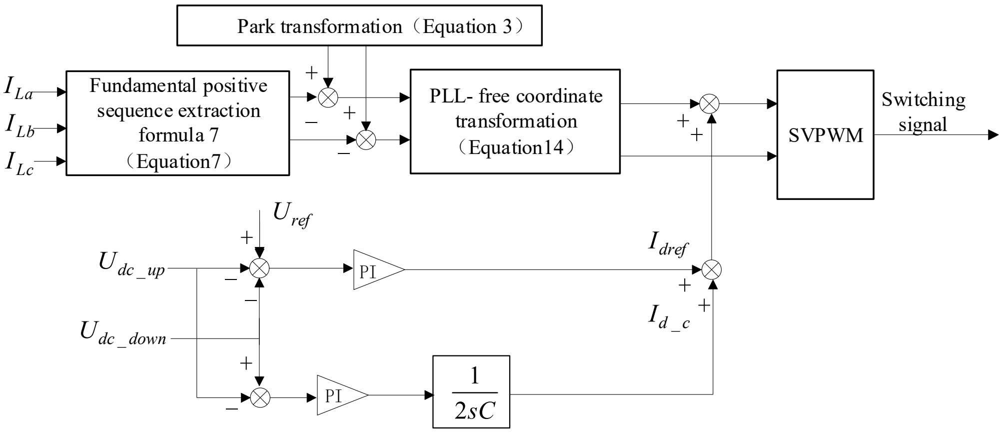

Figure 8. Overall control scheme.

4. SVPWM Method for the Three-Phase Four-Switch Topology

The space vector diagram for the three-phase four-switch topology is shown in Figure 9. The inverse tangent function of the target voltage vector U_{ref} can be used as the sector division criterion of the SVPWM algorithm for the three-phase four-switch APF.

$$\delta = \arctan\left(u_\beta / u_\alpha\right) \tag{21}$$

where δ is the angle of the target voltage vector. The sector of the target voltage vector is chosen according to δ. The interval of δ is within $(-\pi/2, +\pi/2)$ and does not correspond to the angle of a complete cycle.

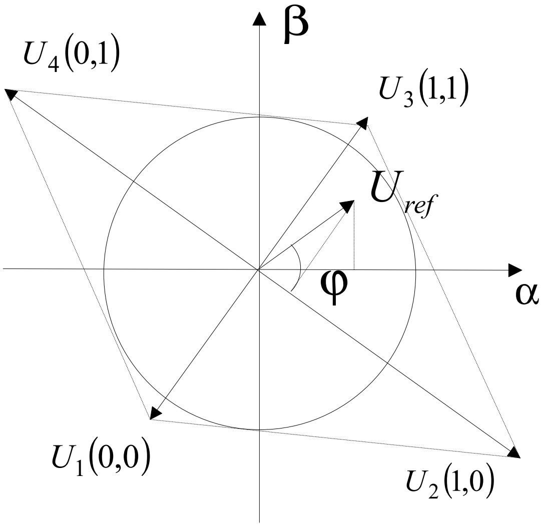

Figure 9. Diagram of a basic voltage vector.

To accurately determine the target voltage sector, the target voltages U_1, U_2, U_3, and U_4 are rotated counterclockwise by $2\pi/3$ radians using rotating coordinates, thus obtaining a new coordinate system. Then, according to the sector δ quadrant, the voltage sector is obtained as shown in Figure 10.

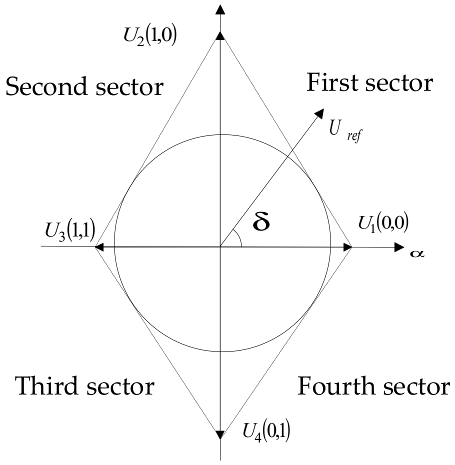

Figure 10. Diagram of a basic voltage vector in a rotated coordinate frame.

The rotated coordinate equation is as follows:

$$\begin{bmatrix} U_{\alpha} \\ U_{\beta} \end{bmatrix} = \begin{bmatrix} \cos(-2\pi/3) & -\sin(-2\pi/3) \\ \sin(2\pi/3) & \cos(2\pi/3) \end{bmatrix} \begin{bmatrix} U'_{\alpha} \\ U'_{\beta} \end{bmatrix} \tag{22}$$

The state of the voltage vector in the new coordinate frame is shown in Table 1 below.

Table 1. Voltage vector states in the rotated coordinate system.

Voltage Vector	S_a	S_a	U_s
U_1	0	0	$\left(U_{dc}/\sqrt{6}\right)e^{j0}$
U_2	1	0	$\left(U_{dc}/\sqrt{2}\right)e^{j(\pi/2)}$
U_3	1	1	$\left(U_{dc}/\sqrt{6}\right)e^{j\pi}$
U_4	0	1	$\left(U_{dc}/\sqrt{2}\right)e^{j(2\pi/3)}$

If N = 1*A + 2*B + 3*C + 4*D and $0 \leq \delta < \frac{\pi}{2}$, then A = 1; otherwise, A = 0. Similarly, if $\frac{\pi}{2} \leq \delta < \pi$, then B = 1; otherwise, B = 0. If $\pi \leq \delta < \frac{3\pi}{2}$, then C = 1; otherwise, C = 0. If $\frac{3\pi}{2} \leq \delta < 2\pi$, then D = 1; otherwise, D = 0. The relationship between N and the sectors is shown in Table 2.

Table 2. Relationship between N and the sectors.

N	**Disk Sector (Computing)**
1	1
2	2
3	3
4	4

According to the analysis, the target vector U_{ref} should be synthesized by the base voltage vectors U_1, U_2, U_3, and U_4, meeting the following equation:

$$\left|U_{ref}\right|T_s = |U_1|T_1 + |U_2|T_2 + |U_3|T_3 + |U_4|T_4 \tag{23}$$

where T_1, T_2, T_3, and T_4 are the work time of the base voltage vectors U_1, U_2, U_3, and U_4, respectively, and T_S is the switching cycle time. The following is true:

$$T_s = T_1 + T_2 + T_3 + T_4 \tag{24}$$

A zero vector is needed to synthesize the target vector. However, in a three-phase four-switch circuit, there are only four basic voltage vectors and no zero vector. The two smallest basic voltage vectors, i.e., U_1 and U_3, are taken to synthesize the zero vector, making up for its absence. If we take the first sector as an example, as shown in Figure 11, U_{ref}, the target voltage, can be expressed as follows:

$$\begin{cases} \left|U_{ref}\right||\cos\delta|T_s = {T_1}^1|U_1| \\ \left|U_{ref}\right||\sin\delta|T_s = T_2|U_2| \end{cases} \tag{25}$$

where δ is the angle between the target voltage U_{ref} and the base voltage vector U_1, ${T_1}^1$ is the time taken to generate U_{ref} by U_1, and T_2 is the time taken to generate U_{ref} by U_2.

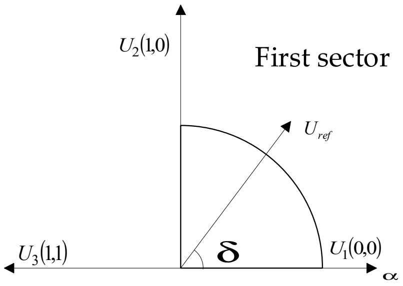

Figure 11. Vector diagram of voltage in the first sector.

As mentioned above, using U_1 and U_3 to synthesize an equivalent zero vector, the two vectors are equal in magnitude, and the relationship between the times can be introduced as follows:

$$\begin{cases} {T_1}^2 = T_3 \\ T_0 = {T_1}^2 + T_3 \\ T_0 = T_s - {T_1}^1 - T_2 \end{cases} \tag{26}$$

where T_3 is the time taken to synthesize the zero vector by U_3, ${T_1}^2$ is the time taken to synthesize the zero vector by U_1, and T_0 is the total work time taken to synthesize the equivalent zero vector.

Combining Equation (25) with (26), the time is derived as follows:

$$\begin{cases} T_1 = \dfrac{T_s - T_2 + \frac{\left|U_{ref}\right|}{|U_1|}|\cos\delta|T_s}{2} \\ T_2 = \dfrac{\left|U_{ref}\right|}{|U_2|}|\sin\delta|T_s \\ T_3 = \dfrac{T_s - T_2 - \frac{\left|U_{ref}\right|}{|U_1|}|\cos\delta|T_s}{2} \end{cases} \tag{27}$$

The operation time of each base voltage vector in the first sector can be obtained from Equation (27). According to the principle of vector concentration, the effective vectors work at the start and end of the control period, while the zero vector works in the middle. In sector one, the target vector U_{ref} is synthesized by U_1, U_2, and U_3. U_1 and U_2 synthesize the effective vector, while U_1 and U_3 synthesize the zero vector. The working order is U_2, U_1, U_3, U_1, and U_2 and the corresponding action times are $T_2/2$, $T_1/2$, T_3, $T_1/2$, and $T_2/2$. The voltage vector's working time in the other three sectors is same as in the first sector. The voltage vector is obtained in the sectors as shown in Table 3.

Table 3. Voltage vector working time.

Sector	Order	Time
First sector	U_2, U_1, U_3, U_1, U_2	$T_2/2, T_1/2, T_3, T_1/2, T_2/2$
Second sector	U_2, U_3, U_1, U_3, U_2	$T_2/2, T_3/2, T_1, T_3/2, T_2/2$
Third sector	U_4, U_3, U_1, U_3, U_4	$T_4/2, T_3/2, T_1, T_3/2, T_4/2$
Fourth sector	U_4, U_1, U_3, U_1, U_4	$T_4/2, T_1/2, T_3, T_1/2, T_4/2$

To maintain the SVPWM algorithm's symmetry and smoothness, the time of the switching mode transition within the first sector can be presented as shown in Figure 12.

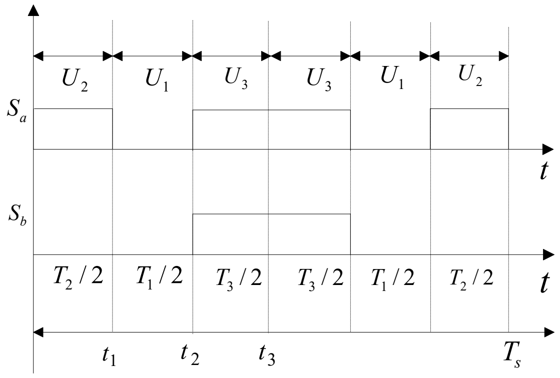

Figure 12. Switching vector timing diagram.

At $0 - t_1$, S_a = 1 and S_b = 0. S_1 and S_4 are on, while S_2 and S_3 are off. At $t_1 - t_2$, S_a = 0 and S_b = 0. S_3 and S_4 are on, while S_1 and S_2 are off. S_1 and S_3 switch at t_1. At $t_2 - t_3$, S_a = 1 and S_b = 1. S_1 and S_2 are on, while S_3 and S_4 are off. S_1 and S_3 switch at t_2. Therefore, the point of switching mode shift within the first sector is as follows:

$$\begin{cases} T_{a1} = \frac{T_2}{2} \\ T_{a2} = \frac{T_1+T_2}{2} \\ T_b = \frac{T_1+T_2}{2} \end{cases} \tag{28}$$

where T_{a1} and T_{a2} are the switching times for switches S_1 and S_3 in the bridge arm, while T_b is that for switches S_2 and S_4 in the bridge arm. The basic voltage vector working time can be obtained from the calculation of the first sector, as shown in Table 4.

Table 4. Switching time in different sectors.

Sector	First Sector	Second Sector	Third Sector	Fourth Sector
T_a	$\frac{T_2}{2}, \frac{T_1+T_2}{2}$	$\frac{T_2+T_3}{2}$	$\frac{T_4}{2}, \frac{T_3+T_4}{2}$	$\frac{T_1+T_4}{2}$
T_b	$\frac{T_1+T_2}{2}$	$\frac{T_2}{2}, \frac{T_2+T_3}{2}$	$\frac{T_3+T_4}{2}$	$\frac{T_4}{2}, \frac{T_1+T_4}{2}$

5. Simulation Analysis

To verify the method proposed in this paper, we carried out a simulation of the three-phase four-switch APF without PLL based on fundamental positive sequence extraction. The nonlinear load was composed of the uncontrollable rectifier bridge with a resistor and an inductor. The relevant simulation parameters are summarized in Table 5.

Table 5. Simulation parameters.

Parameter	Value
Grid voltage and frequency	380 V, 50 Hz
Nonlinear load	5 Ω, 2 mH
Filter inductors	2 mH
DC voltage	1600 V
Capacitance on DC side	5000 µF

Figure 13 shows the whole DC voltage when the system is running. The bus voltage fluctuation on the DC side is very small, maintaining a maximum deviation value within 2 V. The whole voltage can remain stable around 1600 V.

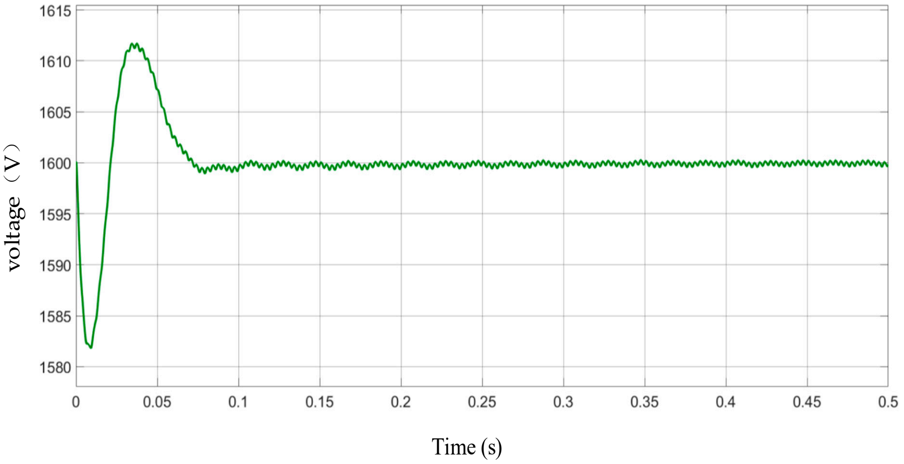

Figure 13. Simulation waveform of the voltage on the DC side.

The two-split capacitance voltage on the DC side is shown in Figure 14. The voltage of the two capacitors is stable at about 800 V, maintaining maximum fluctuation deviations within ±2 V.

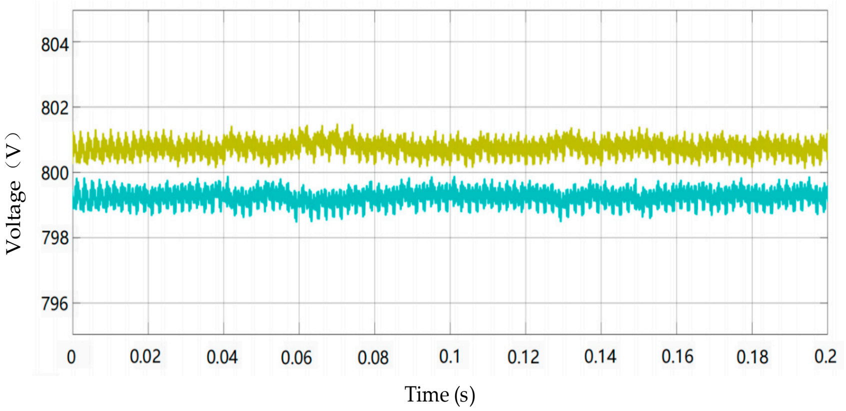

Figure 14. Simulation waveform of the voltage on the DC side.

The source current waveform is shown in Figure 15. The three-phase four-switch active power filter starts working at 0.05 s, prior to which the source current is seriously distorted. Under the proposed control strategy, the harmonic is compensated, and the source current turns into symmetrical sine waveforms.

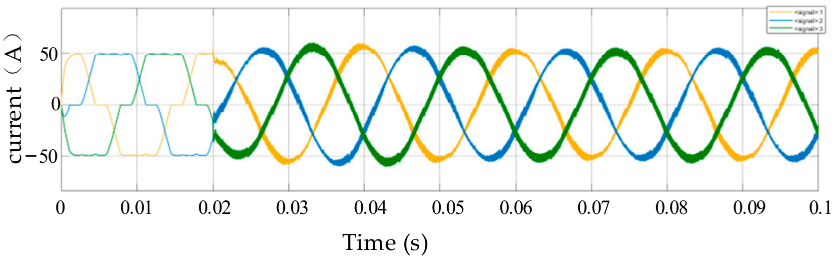

Figure 15. Simulation waveform of the source current.

FFT analysis of the source current is shown in Figure 16. The total harmonic distortion (THD) is 24.72% without a filter. The harmonic is significantly suppressed with a working active filter, and THD is reduced to 3.86%. The proposed method satisfactorily eliminates the harmonic in the power grid.

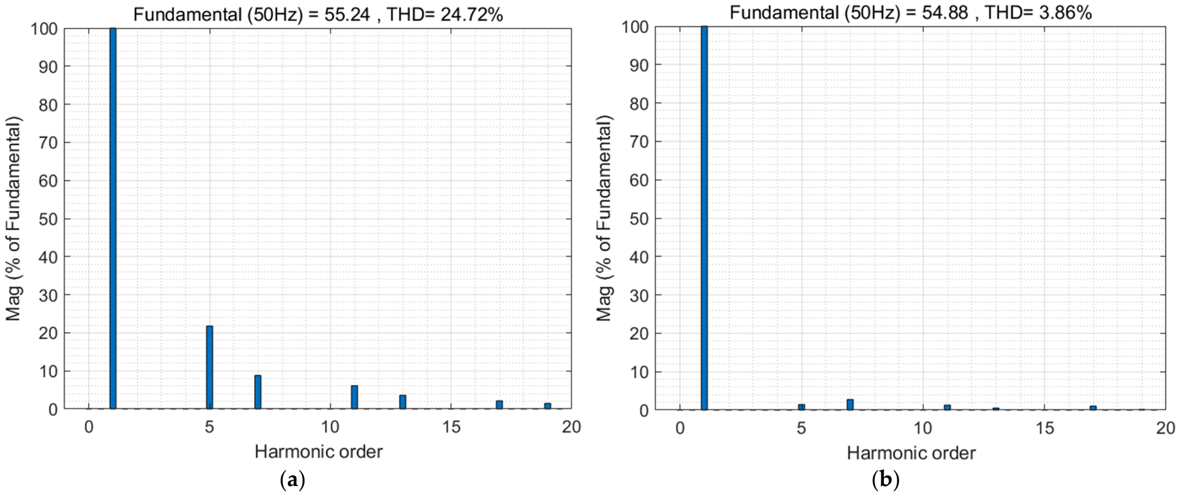

Figure 16. FFT of the source current with (**b**) and without (**a**) the proposed APF.

6. Experimental Results

To verify the above analysis and the proposed control strategy, a dSPACE1004-based experimental platform, shown in Figure 17, was established. The hardware comprised two insulated gate bipolar transistors (FF150R12RT4) and two split capacitors. The experimental parameters are presented in Table 6.

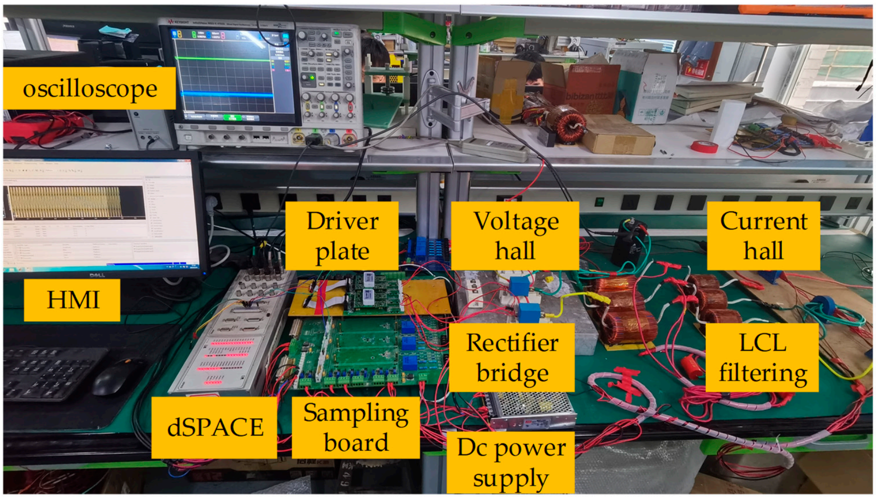

Figure 17. Experimental platform.

Table 6. Experimental parameters.

Parameter	Value
Grid voltage and frequency	50 V,50 Hz
Nonlinear load	5 Ω, 2 mH
Filter inductors	3 mH
DC voltage	800 V
Capacitance on DC side	5000 µF

Figure 18 shows the waveform of the three-phase voltage and current before compensation, along with the i_{sa} Fourier spectrum. It can thus be seen that the source current primarily contains fifth and seventh harmonics. Figure 19 presents the waveforms of the three-phase voltages and currents after compensation, along with the i_{sa} Fourier spectrum. Compared to Figure 18, the source current is regulated into a sinusoidal waveform, with suppressed harmonic components.

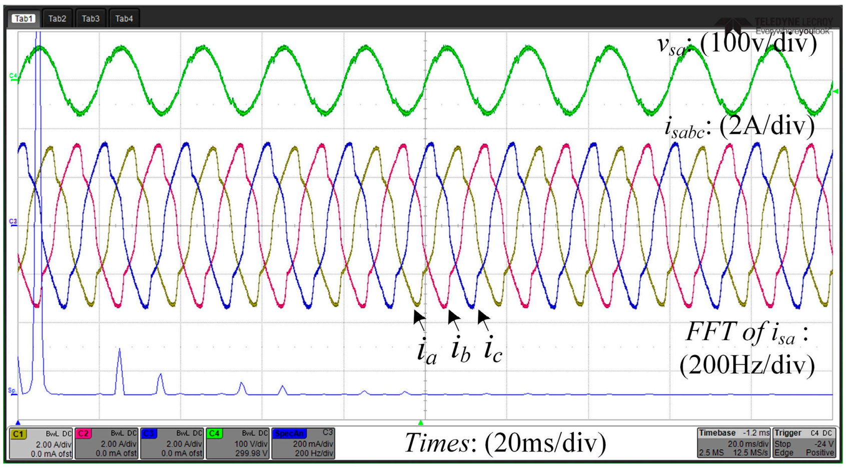

Figure 18. Experimental waveform of AC voltage and current before compensation.

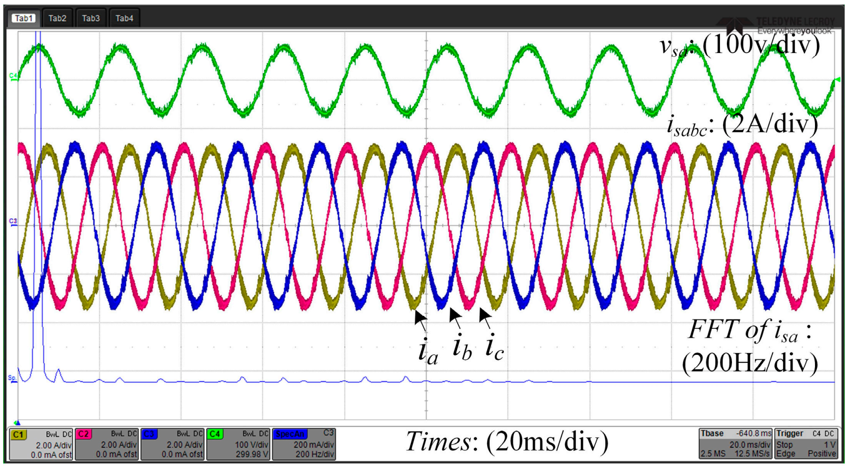

Figure 19. Experimental waveform of AC voltage and current after compensation.

Figure 20 shows the experimental waveform of the DC voltage, averaging 796 V.

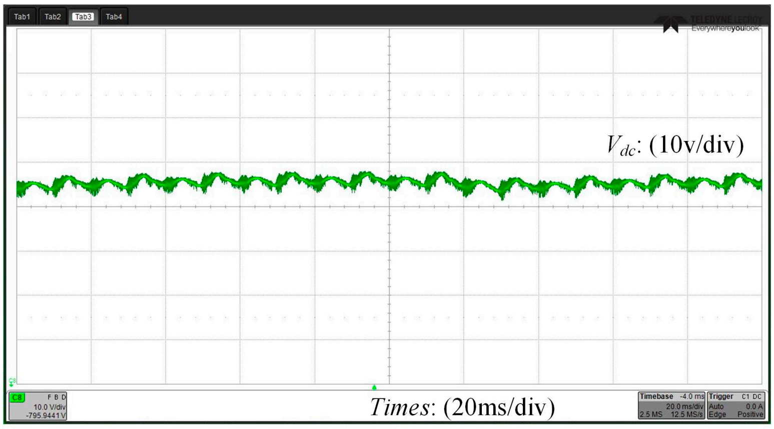

Figure 20. Experimental waveform of the DC voltage.

To investigate the dynamic response to the start and load variations, experiments involving startup and sudden load changes were conducted. Figure 21 shows the transient process during APF startup, with i_{fa} responding rapidly to compensate the harmonic currents. Additionally, during the startup process, i_{sa} remains stable without a startup shock. When APF operates in a steady state, the loads change, and the transient process is shown in Figure 22. It can be seen that the proposed control strategy has a good response to load variations, and i_{sa} is regulated without a shock, rapidly returning to a steady state.

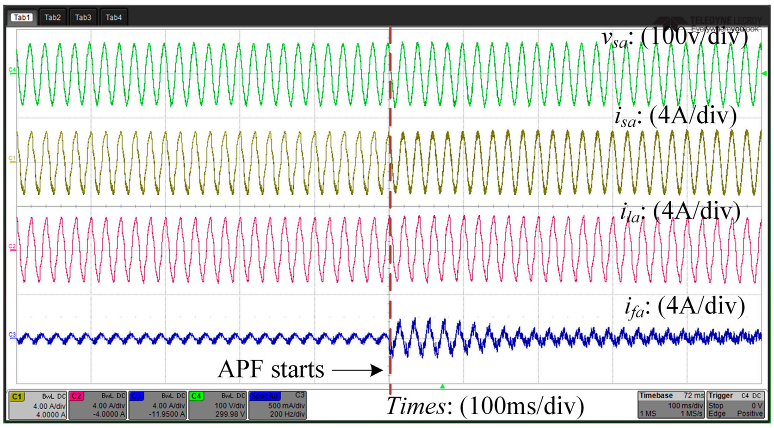

Figure 21. Transient experimental waveforms when the proposed OCC-based APF is applied.

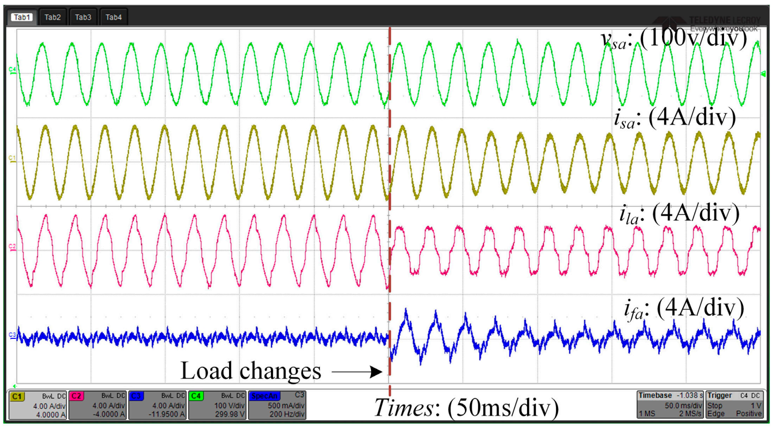

Figure 22. Transient experimental waveforms when the load changes.

To investigate computational efficiency and validate execution time improvements, a DSP TMS320F28377D-based experimental platform was established, with TMS320F28377D able to provide a signal processing performance of 200 MHz. The computation cycles and execution times of the SRF and proposed method in DSP were measured in Code Composer Studio using the clock tool: the former's core algorithm required roughly 6106 clock cycles, while the latter only needed approximately 4362. Assuming that each instruction cycle in DSP was 5 ns, the SRF method required 30.53µs to run, whereas the proposed method only needed approximately 21.81 µs. The proposed method was thus shown to have a shorter computation time and less computations.

7. Conclusions

APFs are an effective approach to solving harmonic problems in power grids, and their control strategy plays a crucial role in improving the power quality. The three-phase four-switch topology of APFs has attracted more attention due to its fewer semiconductors and lower costs. A modified control strategy for a three-phase four-switch APF based on fundamental positive sequence extraction was proposed in this paper, which removes the PLL and rotating coordinate transformation present in traditional control strategies. We introduced harmonic extraction based on the fundamental positive sequence extraction method, while non-locked phase loop coordinate transformation was developed to eliminate trigonometric calculations. The proposed APF and control strategy have satisfactory performance in suppressing the harmonic, which was confirmed, alongside their effectiveness, via simulation and experiments.

The proposed method offers excellent harmonic compensation for three-phase four-switch APFs, reducing two switches and decreasing computational complexity compared to conventional APFs and control strategies. Harmonic extraction based on fundamental positive sequence extraction guarantees the accuracy of the APF reference current. The coordinate transformation method without a phase-locked loop includes accuracy calculations. The APF's DC voltage remains constant and stable, while that of the two split capacitors is balanced and their difference is significantly reduced. Therefore, three-phase four-switch APFs with the proposed control scheme are a promising alternative.

However, when grid voltages fluctuate, the fundamental positive sequence extraction method proposed in the paper may misjudge or miss certain fundamental components, resulting in inaccurate extraction results. It is particularly prone to occurring when the frequency fluctuations are close to the fundamental frequency, further impacting the extraction accuracy. In addition, when the grid voltage is distorted, conventional PLL-based methods can employ a synchronous reference frame phase-locked loop (SRF-PLL) or a decoupled double-synchronous reference frame phase-locked loop (DDRF-PLL) to improve performance, while the coordinate transformation accuracy could be decreased in the proposed method.

Author Contributions: Conceptualization, C.X. and L.W.; data curation, Q.C.; formal analysis, Y.R.; funding acquisition, Y.R.; investigation, Y.R.; methodology, Y.R.; project administration, J.Y.; software, C.X.; supervision, Q.C. and J.Y.; validation, C.X. and Q.C.; writing—original draft, C.X. and L.W.; and writing—review and editing, C.X. All authors have read and agreed to the published version of the manuscript.

Funding: This work was supported by the Science and Technology Project of STATE GRID Shanxi Electric Power Company "Analysis of the Impact Mechanism and Accuracy Improvement of Electric Energy Measurement for New Type Power Systems" (52051L230002).

Data Availability Statement: The data presented in this study are available upon request from the corresponding author (privacy).

Conflicts of Interest: Chun Xiao, Yulu Ren, and Qiong Cao are employed by the State Grid Shanxi Marketing Service Center company, while Jingyu Yin is employed by the Taiyuan Electric Power Supply Company of State Grid Shanxi Electric Power Company. The remaining authors declare that this research was conducted in the absence of any commercial or financial relationships that could be construed as potential conflicts of interest.

References

1. Liang, X. Emerging Power Quality Challenges Due to Integration of Renewable Energy Sources. *IEEE Trans. Ind. Appl.* **2017**, *53*, 855–866. [CrossRef]
2. Anzalchi, A.; Sundararajan, A.; Moghadasi, A.; Sarwat, A. High penetration grid-tied photovoltaics: Analysis of power quality and feeder voltage profile. *IEEE Ind. Appl. Mag.* **2019**, *25*, 83–94. [CrossRef]
3. Honrubia-Escribano, A.; García-Sánchez, T.; Gómez-Lázaro, E.; Muljadi, E.; Molina-García, A. Power Quality Surveys of Photovoltaic Power Plants: Characterisation and Analysis of Grid-Code Requirements. *IET Renew. Power Gener.* **2015**, *9*, 466–473. [CrossRef]
4. Abdel-Aziz, A.; Elgenedy, M.A.; Williams, B.W. Two-Leg Neutral-Point Diode-Clamped Active Front-End Rectifier. *IEEE J. Emerg. Sel. Top. Power Electron.* **2024**, *12*, 405–419. [CrossRef]
5. Bollen, M.H.; Das, R.; Djokic, S.; Ciufo, P.; Meyer, J.; Rönnberg, S.K.; Zavodam, F. Power Quality Concerns in Implementing Smart Distribution-Grid Applications. *IEEE Trans. Smart Grid* **2017**, *8*, 391–399. [CrossRef]
6. Peng, F.Z.; Lai, J.S. Reactive Power and Harmonic Compensation Based on the Generalized Instantaneous Reactive Power Theory for Three-phase Power Systems. In Proceedings of the 7th International Conference on Harmonics and Quality of Power, Las Vegas, NV, USA, 16 October 1996; pp. 83–89.
7. Hirofumi, A.; Yoshihira, K.; Akira, N. Instantaneous Reactive Power Compensators Comprising Switching Devices without Energy Storage Components. *IEEE Trans. Ind. Appl.* **1984**, *IA-20*, 625–630.
8. Gong, C.; Cheng, Z.; Sou, W.K.; Lam, C.S.; Chow, M.Y. Collaborative Distributed Optimal Control of Pure and Hybrid Active Power Filters in Active Distribution Network. *IEEE Trans. Power Deliv.* **2023**, *38*, 2326–2337. [CrossRef]
9. Fan, Y.; Zhou, Q.; Wang, J.; Mu, S.; Wang, L. Application of Superconducting-Magnetic-Energy-Storage-Based Current-Source Active Power Filter in Photovoltaics for Harmonic Mitigation. *IEEE Trans. Appl. Supercond.* **2021**, *31*, 1–4. [CrossRef]
10. Li, D.; Wang, T.; Pan, W.; Ding, X.; Gong, J. A Comprehensive Review of Improving Power Quality Using Active Power Filters. *Electr. Power Syst. Res.* **2021**, *199*, 107389. [CrossRef]
11. Gandoman, F.H.; Ahmadi, A.; Sharaf, A.M.; Siano, P.; Pou, J.; Hredzak, B.; Agelidis, V.G. Review of FACTS Technologies and Applications for Power Quality in Smart Grids with Renewable Energy Systems. *Renew. Sustain. Energy Rev.* **2018**, *82*, 502–514. [CrossRef]
12. Rachit, A.; Sood, V.K. Development of EMTP-based active filter model for distribution system studies. In Proceedings of the IEEE Canadian Conference on Electrical and Computer Engineering, Waterloo, ON, Canada, 25–28 May 1998; Volume 1, pp. 77–80.
13. Kesler, M.; Ozdemir, E. Synchronous-Reference-Frame-Based Control Method for UPQC Under Unbalanced and Distorted Load Conditions. *IEEE Trans. Ind. Electron.* **2011**, *58*, 3967–3975. [CrossRef]
14. Serra, F.M.; Montoya, O.D.; De Angelo, C.H.; Forchetti, D.G. On The Use of The P-Q Theory for Harmonic Current Cancellation with Shunt Active Filters. *Adv. Electr. Electron. Eng.* **2019**, *17*, 262–269. [CrossRef]
15. Masiha, A.; Ikhlaq, H.; Shameem, A.L.; Mukul, C. GRLF-LAD Control Based Active Power Filter Operation With QSG-SOGI Algorithm for Grid Voltage Harmonics Disturbance Rejection. *IEEE Access* **2023**, *11*, 135753–135763.
16. Asiminoaei, L.; Blaabjerg, F.; Hansen, S. Detection Is Key—Harmonic Detection Methods for Active Power Filter Applications. *IEEE Ind. Appl. Mag.* **2007**, *13*, 22–33. [CrossRef]
17. Rai, K.B.; Kumar, N.; Singh, A. Three-Phase Grid Connected Shunt Active Power Filter Based on Adaptive Q-LMF Control Technique. *IEEE Trans. Power Electron.* **2024**, *39*, 10216–10225. [CrossRef]
18. Karbasforooshan, M.S.; Monfared, M. Adaptive Self-Tuned Current Controller Design for an LCL-Filtered LC-Tuned Single-Phase Shunt Hybrid Active Power Filter. *IEEE Trans. Power Deliv.* **2022**, *37*, 2747–2756. [CrossRef]
19. Mykhailo, A.; Vasyl, C.; Serhii, P.; Valerii, M.; Ivan, S. Integral Power Theory and Active Filtering Using the α-β Reference Frame. *IEEE Access* **2024**, *12*, 60004–60014.
20. Ferreira, S.C.; Gonzatti, R.B.; Pereira, R.R.; da Silva, C.H.; da Silva, L.E.B.; Lambert-Torres, G. Finite Control Set Model Predictive Control for Dynamic Reactive Power Compensation with Hybrid Active Power Filters. *IEEE Trans. Ind. Electron.* **2018**, *65*, 2608–2617. [CrossRef]
21. Komurcugil, H.; Bayhan, S.; Guler, N.; Blaabjerg, F. An Effective Model Predictive Control Method with Self-Balanced Capacitor Voltages for Single-Phase Three-Level Shunt Active Filters. *IEEE Access* **2021**, *9*, 103811–103821. [CrossRef]
22. Iqbal, M.; Jawad, M.; Jaffery, M.H.; Akhtar, S.; Rafiq, M.N.; Qureshi, M.B.; Ansari, A.R.; Nawaz, R. Neural Networks Based Shunt Hybrid Active Power Filter for Harmonic Elimination. *IEEE Access* **2021**, *9*, 69913–69925. [CrossRef]
23. Kumar, R.; Bansal, H.O.; Gautam, A.R.; Mahela, O.P.; Khan, B. Experimental Investigations on Particle Swarm Optimization Based Control Algorithm for Shunt Active Power Filter to Enhance Electric Power Quality. *IEEE Access* **2022**, *10*, 54878–54890. [CrossRef]
24. Behnam, A.; Hasan, R.; Mohammad, P. A New Fractional-Order Proportional-Resonant Control of Shunt Active Power Filter Based on Genetic Algorithm Optimization. *IEEE J. Emerg. Sel. Top. Power Electron.* **2024**, *12*, 4612–4622.
25. Basha, S.G.; Mani, V.; Mopidevi, S. Single-phase Thirteen-level Dual-boost Inverter Based Shunt Active Power Filter Control Using Resonant and Fuzzy Logic Controllers. *CSEE J. Power Energy Syst.* **2022**, *8*, 849–863.

26. Çelik, D.; Ahmed, H.; Meral, M.E. Kalman Filter-Based Super-Twisting Sliding Mode Control of Shunt Active Power Filter for Electric Vehicle Charging Station Applications. *IEEE Trans. Power Deliv.* **2023**, *38*, 1097–1107. [CrossRef]
27. Fei, J.; Yang, J. Chebyshev Fuzzy Neural Network Super-Twisting Terminal Sliding-Mode Control for Active Power Filter. *IEEE Internet Things J.* **2023**, *10*, 13587–13600. [CrossRef]
28. Serra, F.M.; De Angelo, C.H. Direct Power Control of a Shunt Active Power Filter Using a Modified IDA–PBC Approach with Integral Action. *IEEE Trans. Circuits Syst. II Express Briefs* **2023**, *70*, 1991–1995. [CrossRef]
29. Chawda, G.S.; Shaik, A.G.; Mahela, O.P.; Padmanaban, S.; Holm-Nielsen, J.B. Comprehensive review of distributed FACTS control algorithms for power quality enhancement in utility grid with renewable energy penetration. *IEEE Access* **2020**, *8*, 107614–107634. [CrossRef]
30. Khodabakhsh, J.; Moschopoulos, G. A Four-Switch Three-Phase AC– DC Converter with Galvanic Isolation. *IEEE Trans. Power Electron.* **2020**, *35*, 1699–1710. [CrossRef]
31. Shanmugam, S.K.; Ramachandran, S.; Arumugam, S.; Pandiyan, S.; Nayyar, A.; Hossain, E. Design and Implementation of Improved Three Port Converter and B4-Inverter Fed Brushless Direct Current Motor Drive System for Industrial Applications. *IEEE Access* **2020**, *8*, 149093–149112. [CrossRef]
32. Tareen, W.U.K.; Mekhielf, S. Three-Phase Transformerless Shunt Active Power Filter with Reduced Switch Count for Harmonic Compensation in Grid-Connected Applications. *IEEE Trans. Power Electron.* **2018**, *33*, 4868–4881. [CrossRef]
33. Aboutaleb, A.M.; Azazi, H.Z.; Osheba, D.S.M.; El-Abbe, A.E. Active Power Filter with Reduced Number of Semiconductor Switches Based on Synchronous Reference Frame. In Proceedings of the 2019 IEEE Conference on Power Electronics and Renewable Energy (CPERE), Aswan, Egypt, 23–25 October 2019; pp. 151–155.
34. Trinh, Q.N.; Lee, H.H. An Advanced Current Control Strategy for Three-Phase Shunt Active Power Filters. *IEEE Trans. Ind. Electron.* **2013**, *60*, 5400–5410. [CrossRef]
35. Joos, G.; Chen, S.; Haddad, K. Four Switch Three Phase Active Filter with Reduced Current Sensors. In Proceedings of the 2000 IEEE 31st Annual Power Electronics Specialists Conference. Conference Proceedings, Galway, Ireland, 23 June 2000; pp. 1318–1323.
36. Abdel-Aziz, A.Z.; Elgenedy, M.A.; Williams, B.W. Model Predictive Current Control for Low-Cost Shunt Active Power Filter. *CSEE J. Power Energy Syst.* **2024**, *10*, 1589–1598.
37. Bala, S.; Patel, N.; Femandes, B.G. Reduced-Switch Three-Phase Active Power Filter with One Cycle Control. In Proceedings of the 2004 IEEE 35th Annual Power Electronics Specialists Conference, Aachen, Germany, 20–25 June 2004; pp. 2333–2339.
38. Komurcugil, H.; Kukrer, O. A Double-Band Hysteresis Control Approach for Three-Phase Four-Switch Active Filters with Switching Frequency Mitigation. In Proceedings of the IECON 2014–40th Annual Conference of the IEEE Industrial Electronics Society, Dallas, TX, USA, 29 October–1 November 2014; pp. 1021–1027.
39. Biricik, S.; Komurcugil, H. Three-Level Hysteresis Current Control Strategy for Three-Phase Four-Switch Shunt Active Filters. *IET Power Electron.* **2016**, *9*, 1732–1740. [CrossRef]
40. Hoseinpour, A.; Ghazi, R. Using of A Three-Phase Four-Switch Inverter Equipped with A Variable Index PWM to Improve The Power Quality of A Wind Power Plant. *Int. J. Ind. Electron. Control Optim.* **2020**, *3*, 213–222.